

## Recovery Processes and Factors Limiting Cloud-Top Height following the Arrival of a Dry Intrusion Observed during TOGA COARE

J.-L. REDELSPERGER

*Centre National de Recherches Météorologiques, Météo-France and CNRS, Toulouse, France*

D. B. PARSONS

*Atmospheric Technology Division, National Center for Atmospheric Research,\* Boulder, Colorado*

F. GUICHARD

*Centre National de Recherches Météorologiques, Météo-France and CNRS, Toulouse, France*

(Manuscript received 16 August 2001, in final form 19 February 2002)

### ABSTRACT

This study investigates the recovery of the tropical atmosphere to moist conditions following the arrival of a dry intrusion observed during the Tropical Ocean and Global Atmosphere Program Coupled Ocean–Atmosphere Response Experiment (TOGA COARE). A cloud-resolving model was used to quantify the processes leading to the moistening of the lower and middle troposphere. The model replicates the general recovery of the tropical atmosphere. The moisture field in the lower and middle troposphere recovered in large part from clouds repeatedly penetrating into the dry air mass. The moistening of the dry air mass in the simulation was due to lateral mixing on the edges of cloudy regions rather than mixing at cloud top. While the large-scale advection of moisture played a role in controlling the general evolution of moisture field, the large-scale thermal advection and radiation tend to directly control the evolution of the temperature field. The diurnal variations in these two terms were largely responsible for temperature variations above the boundary layer. Thermal inversions aloft were often found at the base of dry layers.

The study also investigates which factors control cloud-top height for convective clouds. In both the observations and simulation, the most common mode of convection was clouds extending to ~4–6 km in height (often termed cumulus congestus clouds), although the period also exhibited a relatively wide range of cloud tops. The study found that cloud-top height often corresponded to the height of the thermal inversions. An examination of the buoyancy in the simulation suggested that entrainment of dry air decreased the parcel buoyancy making these inversions more efficient at controlling cloud top. Water loading effects in the simulation were generally secondary. Thus, there is a strong coupling between the dry air and thermal inversions as clear-air radiative processes associated with the vertical gradient of water vapor produce these inversions, while inversions and entrainment together limit the vertical extent of convection. One positive impact of dry air on convection occurred early in the simulation when clouds first penetrate the extremely dry air mass just above the boundary layer. At this time in the simulation, water vapor excesses within the rising parcels strongly contributed to the positive buoyancy of the clouds. In general, however, the impacts of dry air are to limit the vertical extent of convection and weaken the vertical updrafts.

### 1. Introduction

The appearance of extremely dry air over the tropical western Pacific has received a great deal of attention in recent years (e.g., Parsons et al. 1994; Numaguti et al. 1995; Yoneyama and Fujitani 1995; Mapes and Zuidema

1996; Johnson et al. 1996; Sheu and Liu 1995; DeMott and Rutledge 1998; Yoneyama and Parsons 1999; Parsons et al. 2000). These dry air events are termed dry intrusions, since the dry air originates aloft at higher latitudes and subsides into the Tropics in long filaments, several hundred kilometers in width. It is thus now quite established that this dry air is not a consequence of convection but, rather, it affects the behavior of convection and precipitation. These extreme events were apparently unknown before the Tropical Ocean Global Atmosphere Coupled Ocean–Atmosphere Response Experiment (TOGA COARE). Recently, Yoneyama and Parsons (1999) showed that the intrusions are related to

---

\* The National Center for Atmospheric Research is sponsored by the National Science Foundation.

---

Corresponding author address: Dr. J.-L. Redelsperger, CNRS/GAME, Avenue Coriolis 42, Toulouse 31057, France.  
E-mail: redels@meteo.fr

Rossby wave breaking and that the dry air could be tracked back in time to the remnant circulation of middle latitude baroclinic waves. They found that dry events were present over the region  $\sim 9\%$  to  $17\%$  of the time during TOGA COARE. Recent examination of 20 yr of meteorological analyses (Waugh and Polvani 2000) shows that dry intrusions originating from the breaking of Rossby waves propagating along the subtropical jet are particularly frequent during the boreal winter. They reported an average of 8 events per boreal winter over the Atlantic and Pacific Oceans, the latter being the dominant region with roughly 6 events per winter. After the arrival of a dry intrusion, the typical timescale for the whole tropical atmosphere to recover to moist conditions is  $\sim 10$  to 20 days, whereas the recovering of the lower and middle troposphere is achieved within a week (Parsons et al. 2000).

It has been established that dry intrusions have a pronounced impact on cloud and radiative processes in the Tropics (e.g., Numaguti et al. 1995; Yoneyama and Fujitani 1995; Johnson et al. 1996; Mapes and Zuidema 1996; Brown and Zhang 1997; DeMott and Rutledge 1998; Parsons et al. 2000). Mapes and Zuidema (1996) discussed the radiative impact of these extremely dry air masses on convective instability over the tropical warm pool in the western Pacific. They noted that the typical vertical profile of longwave cooling was greatly disturbed by the presence of extremely dry air within the middle and lower troposphere. They further proposed that the vertical profile of longwave cooling contributed to a strong thermal inversion at the base of the dry layer. More recently, Parsons et al. (2000) suggested that, since shortwave absorption nearly balances longwave cooling at solar noon, there should be a distinct diurnal variation in the magnitude of these strong inversions. The variation in the magnitude of this inversion, in turn, impacts the convective stability, making the diurnal variation of the clear air radiative forcing an important factor in controlling the diurnal cycle of stability and convection after a dry event over the warm pool. The changes in the cloud layers following the arrival of a dry intrusion over the Tropics correspond in an expected way to the predicted changes in the convective stability. For example, studies have found that the appearance of dry air coincides with the suppression of deep convection (Brown and Zhang 1997; DeMott and Rutledge 1998). The suppression of deep convection can be so pronounced that Brown and Zhang (1997) regarded these periods as tropical droughts. Suppression of deep convection by a dry intrusion could be due to either the increased stability arising from radiative processes or to a reduction in the buoyancy of clouds resulting from mixing with the extremely dry environmental air. As a consequence, it is important to study the atmospheric recovery following a dry intrusion not only in terms of the evolution in moisture, but also in temperature.

The frequency and the dramatic consequences of

these extreme dry events, together with the long adjustment times found in recent cumulus modeling studies (e.g., Tompkins and Craig 1998), suggest that it is difficult for the atmosphere to approach a convective–radiative equilibrium in the presence of these intrusions. Instead, the net effect of these dry periods is that the tropical atmosphere spends a great deal of time recovering from these higher latitude forcings. In summary, dry intrusions are hypothesized to have a large impact over the water vapor budget and consequently on the dynamics of the regions where they occur. Though previous studies have greatly improved our knowledge of dry intrusions, the interplay between clouds and the environment during this crucial period of recovery is not well understood due to the recent discovery of dry intrusions over equatorial regions and the limitations of the available observational datasets. The conceptual model of the recovery process issued by Parsons et al. (2000) based on their extended analysis of observations and the results of previous authors needs to be evaluated. One central hypothesis made in this latter paper was that the re moistening mainly occurred through cloud detrainment. The present study allows testing of this hypothesis through quantification of the different processes involved in the recovery of the moisture field. The conceptual model also outlined the possible role played by the diurnal cycle of convective inhibition (CIN), which may partly be responsible for the unusual diurnal cycle of rainfall observed during this period. These aspects will not be considered in the present paper.

The major goals of this study are twofold: 1) to obtain a quantitative description of the recovery of the lower and middle troposphere following a dry intrusion by distinguishing the various involved processes, and 2) to determine what factors limit the cloud-top height over the tropical western Pacific through examination of the recovery process. A useful tool to achieve the present goals is the cloud-resolving model driven by local and large-scale observations as discussed in section 2. In section 3, numerical results are evaluated against available observations in terms of surface fluxes, rainfall, thermodynamics and cloud evolution. The simulation is subsequently used to establish the contribution of the various processes involved in the atmosphere recovery. Some preliminary findings concerning the diurnal cycle in the water vapor and temperature fields are also described. Section 4 is dedicated to the identification of the respective role of factors limiting cloud-top height.

## 2. Case study and experimental design

The dry intrusion observed during TOGA COARE on 13–20 November 1992 was selected for this study. This event has been the subject of several observational papers (Parsons et al. 1994; Numaguti et al. 1995; Mapes and Zuidema 1996; Brown and Zhang 1997; DeMott and Rutledge 1998; Yoneyama and Parsons 1999; Par-

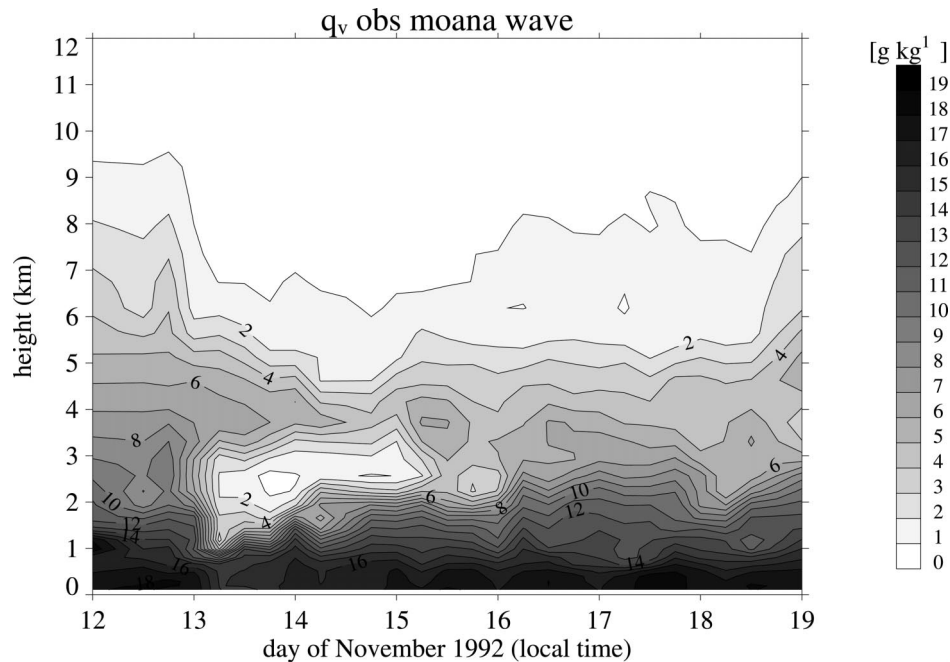


FIG. 1. Time–height cross section of water vapor ( $\text{g kg}^{-1}$ ) as observed from radiosondes launched each 6 h on R/V *Moana Wave*.

sons et al. 2000). The intrusion period also corresponds to a wind transition from westerly to easterly (Lin and Johnson 1996). Figure 1 shows the dramatic dry conditions (specific humidity less than  $1 \text{ g kg}^{-1}$ ) in the layer between 2 and 3.5 km associated with this intrusion and the subsequent slow recovery of the water vapor field. As discussed in Parsons et al. (2000), a secondary drying event aloft (above 5 km) was also observed with specific humidity decreasing by a factor of 2 (e.g., 4 to  $2 \text{ g kg}^{-1}$  at 6 km). With regard to the limited lateral extent of dry intrusion and the entire range of physical processes expected to be involved in the atmospheric recovery (e.g., boundary layer processes, shallow and deep convection), special care needs to be brought into the design of numerical experiments. Thus, this type of case study is believed to be a stringent test for any cloud model, including cloud-resolving models as well as cloud schemes used in general circulation models.

A widely used dataset to drive cloud models for TOGA COARE studies was derived from an objective analysis of TOGA COARE Intensive Flux Array (IFA) measurements by Ciesielski et al. (1997). Due to the lateral size of dry intrusion, only several hundred kilometers in width, the IFA-average profiles of temperature and humidity are not necessarily representative of the local environment at the center of the dry intrusion. In other words, the temperature and moisture fields are strongly inhomogeneous on the IFA scale. For this reason the present simulation was initialized from an individual sounding taken near the middle of the intrusion, rather than with an IFA-average sounding. The IFA-average sounding at this time (not shown) also indicates the

presence of dry air, but with much smaller amplitude. Given that our main objective is to focus on the atmospheric recovery, the simulation was started after the arrival of dry air intrusion. For all these considerations, the present simulation starts from a sounding taken from the R/V *Moana Wave* at  $\sim 2300$  LST on 13 November 1992 (after the arrival of the dry air).

The cloud-resolving model (CRM) utilized in this study is the anelastic nonhydrostatic model of Redelsperger and Sommeria (1986). This model has been extensively used over a wide range of scales to represent squall lines (e.g., Lafore et al. 1988), frontal systems (e.g., Redelsperger and Lafore 1994), and in an earlier version, shallow convection (e.g., Sommeria and LeMone 1978). The model prognostic variables are the three components of the wind, the potential temperature ( $\theta$ ), the specific humidity ( $q$ ), mixing ratios for five hydrometeor species (cloud liquid droplets, rain drops, ice crystals, aggregates, and graupels), and the subgrid turbulent kinetic energy ( $E$ ). Special care has been given to the formulation of parameterized turbulent processes. Based on a prognostic equation for  $E$ , the model utilizes quasi-conservative variables for condensation and incorporates the effect of thermal stratification on subgrid fluxes (Balaji and Redelsperger 1996). A Kessler-type parameterization is used for warm microphysical processes, except for subgrid-scale condensation and conversion from cloud droplets in raindrops (Redelsperger and Sommeria 1986). Ice phase microphysics are treated with the scheme developed by Caniaux et al. (1994), which includes three prognostic equations for the following solid hydrometeors: ice crystals, aggregates, and

graupel. Radiative effects within the model are computed fully interactively with the cloud field using the radiation scheme of the European Centre for Medium-Range Weather Forecasts [ECMWF; Morcrette (1991); see Guichard et al. (1996) for its implementation in the CRM]. Radiative fluxes are computed every 1 and 15 min for cloudy and clear-sky columns, respectively. Surface fluxes are computed with the COARE bulk algorithm, derived from the hourly sea surface temperature (SST) measured on R/V *Moana Wave*. This algorithm includes the effect of boundary layer free convection, but with the proportionality coefficient linking the free convection velocity and the gustiness modified following Redelsperger et al. (2000), whereas the parameterization of gustiness due to deep convection is not included as it is explicitly simulated by the CRM.

The simulation is performed in two-dimensions (2D), due to the considerable cost of three-dimensional (3D) simulations over a 5-day period. Comparison of 2D and 3D simulations by Grabowski et al. (1998) shows that a 2D framework is sufficient to simulate deep convection when, as for the present study, the large-scale forcings are prescribed and the mean wind is nudged towards the observed large-scale wind. The domain size is 100 km along the horizontal axis and 23 km in height. The horizontal grid spacing is 1 km. Numerical tests have shown that the results were not very sensitive to either increasing the horizontal resolution or to the dimensionality of domain (i.e., 2D versus 3D). The horizontal extent is also considered to be sufficiently large, as satellite observations show a lack of deep organized mesoscale convective systems during this suppressed period. The largest systems observed from satellite correspond to isolated convective towers (horizontal extent less than 20 km) with no associated stratiform regions. The vertical grid is stretched, from 70-m resolution in the boundary layer up to 700 m above 10 km. A sponge layer is added above the tropopause, between 16 and 23 km, to avoid spurious reflections. The model integration is done for 5 days with a time step of 12 s.

Cyclic lateral boundary conditions are used so that the advection of temperature and water vapor by the large-scale motion is introduced as an additional term. Following Sommeria (1976), the forcing is applied homogeneously to each column of the simulated domain, as a function of height and time only (see also, Grabowski et al. 1996). The present study uses the large-scale horizontal advection and the large-scale vertical velocity available every 6 h as deduced from COARE observations over the IFA (Ciesielski et al. 1997). We choose to use the large-scale velocity instead of the large-scale vertical advection, due to the large variability in the moisture and temperature fields. Sensitivity tests were made to compare the two methods and will be discussed in the next section. As the large-scale advection terms for the horizontal momentum are not determined accurately enough from the observations, the horizontally averaged winds are nudged toward the ob-

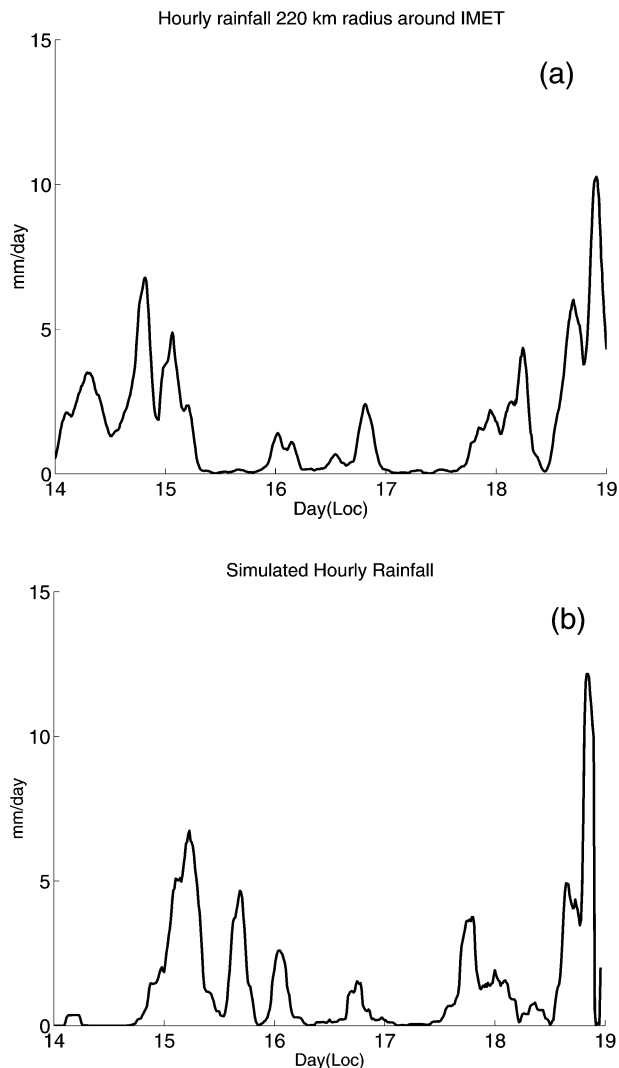


FIG. 2. Hourly rainfall ( $\text{mm day}^{-1}$ ) (a) as estimated from MIT radar over a circle with a 220-km radius, and (b) as simulated by the CRM.

served large-scale values, with a relaxation time of 2 h. Physically this experimental design corresponds to the imposition of the observed large-scale response onto the local conditions observed at the R/V *Moana Wave* near the center of the dry filament.

### 3. General behavior

The design of the experiment with the mean wind over the domain being nudged, the SST being prescribed by observations, and the large-scale advection being tied to the observations suggests that one would hope that the simulation would reproduce the observations. Even with these high expectations, several aspects of the simulation are noteworthy. For example, Figs. 2 and 3 show that the model reproduces reasonably well the general intensity and the timing of rainfall estimated from the radar reflectivity and the observed surface fluxes over

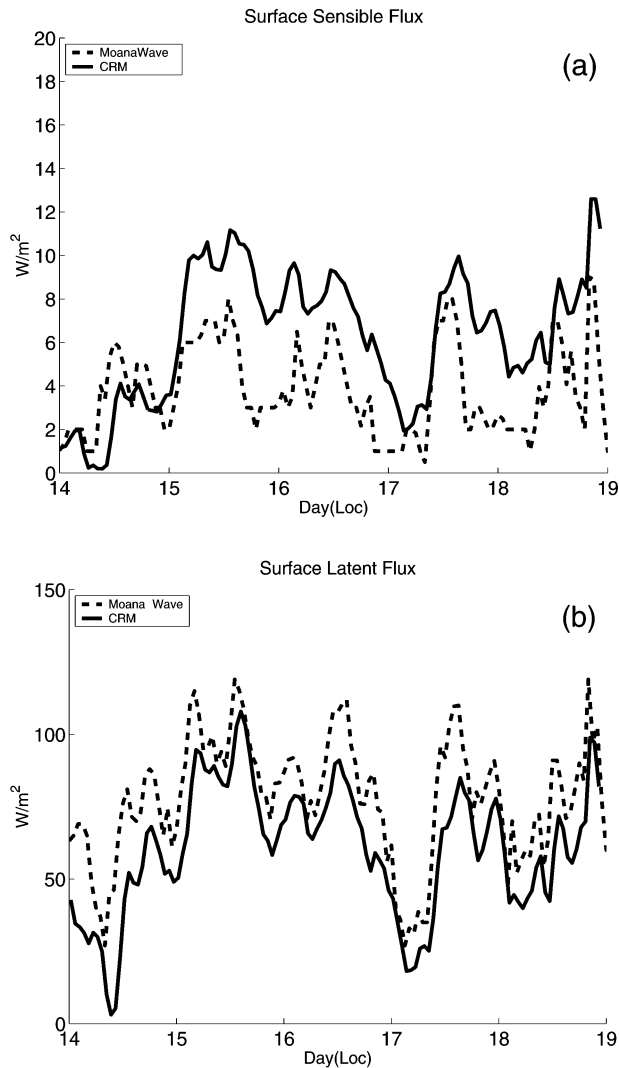


FIG. 3. Surface fluxes as estimated with bulk parameterization from measurements on board the R/V *Moana Wave* (dashed lines) and simulated by the CRM (solid lines): (a) sensible heat flux ( $\text{W m}^{-2}$ ), and (b) latent heat flux ( $\text{W m}^{-2}$ ).

the period. Nevertheless, the model does not capture several observed features. One feature not reproduced is the first observed rainfall event, which occurred during the first 12 h on 14 November (Fig. 2). However, this rainfall event is difficult to reproduce as it is revealed through the satellite and radar data to be quite inhomogeneous with more activity in the southern portion of the domain. The cause of this inhomogeneity is that the dry intrusion arrived with substantial drying in the boundary layer from the south moving toward the north, so that the boundary layer recovered to moist conditions first in the southern portion of the domain. The model initialized with a single sounding north of the precipitation event and forced with horizontal uniform fields is unable to capture this evolution. Another, and perhaps more important, difference between the ob-

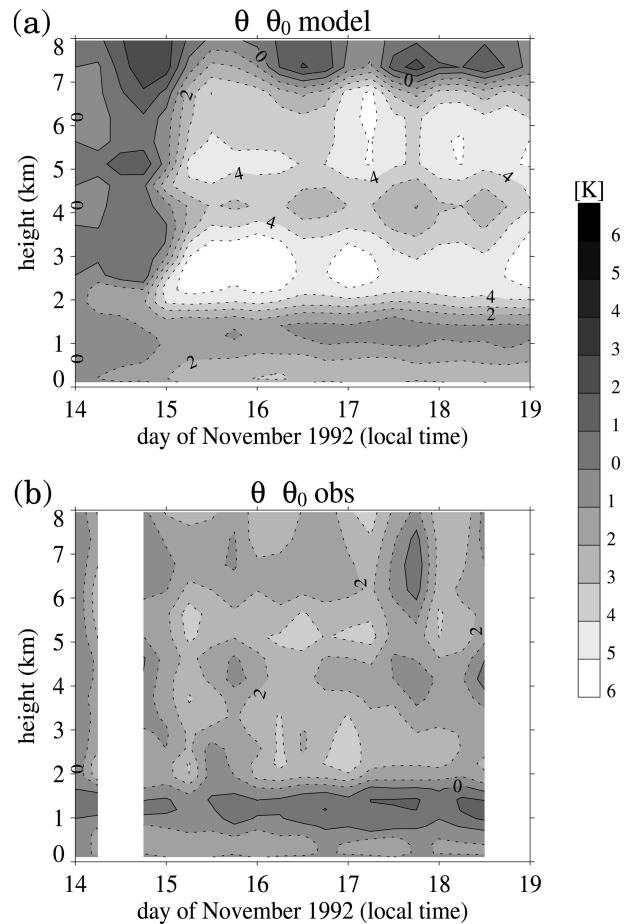


FIG. 4. Differences between potential temperature and initial potential temperature (a) simulated and (b) observed. Contour is 1 K, and simulated fields are averaged over 6 h. White columns in (b) correspond to sonde problems.

servations and the model is that the model appeared to be cool, relative to the observations, by  $\sim 1\text{--}2$  K at the end of the simulation (Fig. 4). This problem has frequently arisen in simulations driven by observed large-scale advectations over this region as found in the second model intercomparison of Global Energy and Water Cycle Experiment (GEWEX) Cloud Systems Studies (GCSS; Krueger et al. 1997). The cause of this problem can come from uncertainties in determining the large-scale advectations, especially the large-scale vertical velocity, as suggested by recent studies (Emanuel and Živković-Rothman 1999; Guichard et al. 2000).

The model accurately reproduced the layering in the moistening (0–0.5 and 1.5–3.5 km) and drying (0.5–1.5 and 3.5–5 km) as shown in Fig. 5. The simulation did tend to overestimate the moistening occurring on 15 November in the vertical layer between 2–3 km. The moisture differences between the radiosonde measurement and the model varied considerably from sounding to sounding, but were generally less than  $1$  to  $2 \text{ g kg}^{-1}$ . Both the model and the observations indicate that a

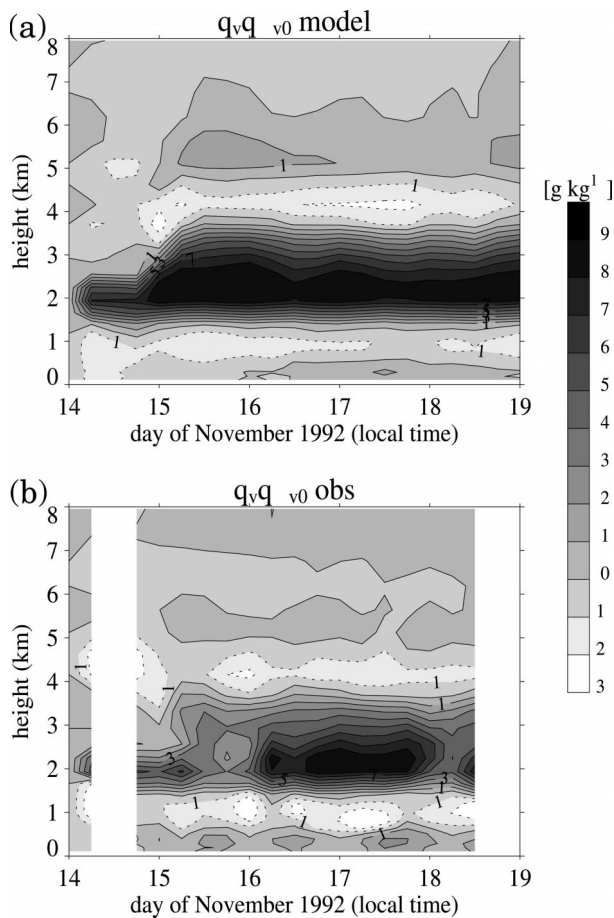


FIG. 5. Same as Fig. 4, except for specific humidity. Contour interval is  $1 \text{ g kg}^{-1}$ .

drying of the atmosphere below the dry intrusion is a part of the recovery process. The drying below the intrusion results from the dry intrusion limiting cloud top and thus decreasing vertical mixing as will be discussed in subsequent sections. Previous studies have generally not noted this drying below the intrusion and instead concentrated on the moistening.

Examination of mean cloud field (Fig. 6) shows that clouds were able to form during almost the entire simulation. At the beginning of the period, large values of CIN<sup>1</sup> in excess of  $70 \text{ J kg}^{-1}$  prevent the triggering of convection. In agreement with the findings of Parsons et al. (2000), the mean CIN in the simulation has a clear tendency to approach small values after 15 November at 1200 LST. The smaller values of CIN slow the development of clouds and likely limit the cloud fraction, rather than prevent cloud formation. The cloud tops generally reached only intermediate levels of the troposphere (between 4 and 6 km), well below the tropopause (around 15 km). These clouds, often referred to as cu-

<sup>1</sup> The CIN is here defined as the amount of energy that must be realized before a parcel can reach its level of free convection.

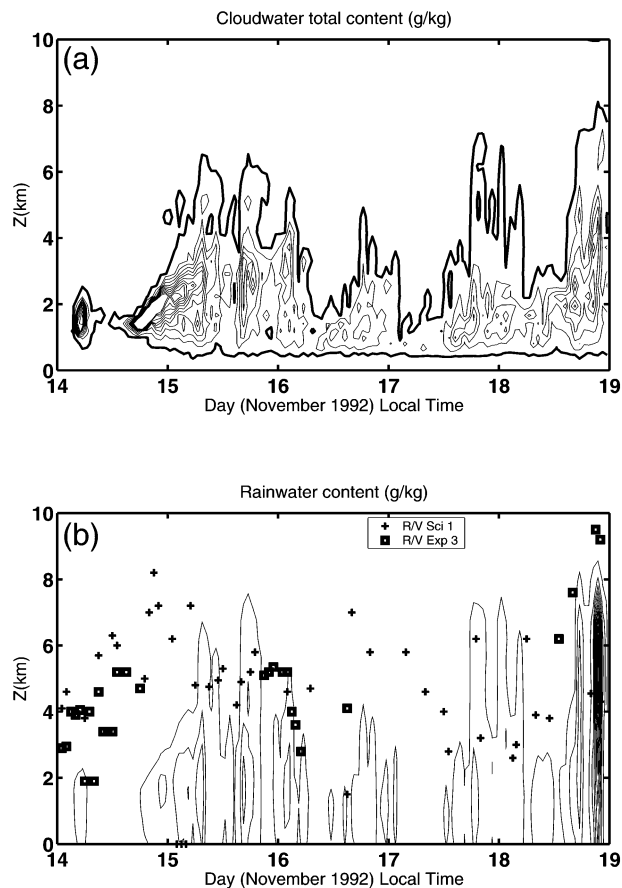


FIG. 6. Time-height cross sections of (a) mean simulated total cloud content (solid isolines) and (b) mean hydrometeor content. Echo tops estimated from reflectivity and from vertical motion fields of the wind profilers on the R/Vs *Sci. #1* and *Exp. #3* are presented in (b).

mulus congestus, appear to be the most common mode of convection throughout the period considered, except during the end of the period when isolated deep convective cells developed. It is worth noting that most of time the clouds are isolated with a mean cloud coverage of  $\sim 10\%$ , except during the last 12 h on 14 November when the cloud coverage varies between 40% and 85%. The echo tops estimated from reflectivity and the vertical motion field from the wind profilers on the R/Vs *Science (Sci.) #1* and *Experiment (Exp.) #3* are presented along with the simulated fields. The wind profilers were deployed as part of an integrated sounding system (ISS) on these vessels (Parsons et al. 1994). The profiler data shows, in broad agreement with the model, a general tendency for clouds reaching only the intermediate levels with the exception of active deep convection at the end of this period. The profiler-derived echo tops also suggest some spatial variations in the nature of convection over the COARE IFA as evidenced by differences between the two sites. For example, from the early hours of 16 November until late in the day on 18 November, conditions are very suppressed at the R/V *Exp.*

#3 and relatively more active at the R/V *Sci. #1*. The behavior of the cloud model is somewhat between these two observed levels of activity. Another example of spatial inhomogeneity is that active deep convection occurs late in the day on 14 November in the vicinity of the southern ship R/V *Sci. #1*, while echo tops are limited to below  $\sim 5.5$  km at the other vessel. As noted earlier, the model has difficulty in replicating convection during this initial period.

The presence of shallow and intermediate clouds during this period, as illustrated with the profiler data and with the simulation, is also consistent with the analysis of radar data from the R/V *Vickers* (DeMott and Rutledge 1998), and the cloud-top distribution deduced from satellite infrared temperature (Brown and Zhang 1997). In a general manner, the behavior of the cloud field also fits with the study of Johnson et al. (1999) showing that cumulus congestus clouds were the most abundant of all precipitating clouds in COARE. During this period the cloud heights imply that much of the rain reaching the surface can be termed as warm rain as the cloud ice phase processes play a secondary role. It seems, thus, that warm rain finds its origin in the existence of factors that limit the vertical extent of convective clouds.

#### 4. The recovery

Dry air intrusions, as stressed by many authors, have a significant impact on the tropical atmosphere. Parsons et al. (2000) proposed a conceptual model of the recovery based on their analysis and insight gained from previous studies (e.g., Nugamuti et al. 1995). The main goal of this section is to evaluate this conceptual model and present a quantitative evaluation of the various processes involved in the recovery. As thermal inversions are typically formed after the arrival of a dry intrusion, the recovery of atmosphere will be studied not only in terms of moisture, but also in terms of temperature. In the conceptual model of Parsons et al. (2000), the boundary layer recovered relatively rapidly from an increase in surface fluxes, while detrainment from shallow cumulus and congestus clouds that reach middle levels slowly moistened the lower and middle troposphere over a timescale of  $\sim 10$  days. The recovery process was nonuniform in the lower and middle levels as these clouds had a diurnal cycle with maximum activity during the evening. The recovery of the upper troposphere took place only after deep convective activity was re-established. Evaluation of this conceptual model is difficult to address solely from the available observations. For example, as evidenced in Figs. 2 and 6 not all clouds lead to precipitating hydrometeors and not all of these hydrometeors reach the ocean surface. In contrast, most of the special observations taken during TOGA COARE are best suited for investigations of precipitating clouds. The cloud model allows for the investigation of the

interaction between the environment and both nonprecipitating and precipitating clouds.

To get insight into the evolution of the vertical profile of potential temperature, its time tendency (Fig. 7a) is decomposed as the sum of the large-scale advection (Fig. 7b), the sum of resolved and subgrid transports (Fig. 7c), the radiative term (Fig. 7d) and the diabatic (phase change) term (Fig. 7e):

$$\begin{aligned} \frac{\partial \theta}{\partial t} = & \left( \frac{\partial \theta}{\partial t} \right)_{\text{LS}} + \left( \frac{\partial \theta}{\partial t} \right)_{\text{Resolved Transport}} \\ & + \left( \frac{\partial \theta}{\partial t} \right)_{\text{Subgrid Transport}} + \left( \frac{\partial \theta}{\partial t} \right)_{\text{Radiation}} \\ & + \left( \frac{\partial \theta}{\partial t} \right)_{\text{Diabatic}}. \end{aligned} \quad (1)$$

In the following discussion, the sum of the model-resolved and subgrid transports will be referred to as the convective transport, which thus includes dry and wet convection occurring in the boundary layer and the free troposphere. During this suppressed regime, the budget terms in Eq. (1) and illustrated in Fig. 7 indicate that the recovery is not a steady process, but instead highly nonuniform, as found in the observed and simulated tendency in the potential temperature. This time tendency for the potential temperature (Fig. 7a) is in turn explained to a large degree above  $\sim 4$  km by the large-scale advection (Fig. 7b). The time series of the large-scale advection appears to have a strong diurnal variation. In actuality, the variation for the first two days is larger and the period longer ( $\sim 1.5$  days). After the first two days, the large-scale advection becomes more diurnal and is primarily driven by the large-scale vertical velocity (not shown) with morning subsidence in agreement with the recent study of suppressed periods by Parsons et al. (2002, manuscript submitted to *J. Atmos. Sci.*). In the simulation, the vertical structure of the large-scale forcing of potential temperature is due to the presence of marked temperature inversions as discussed in the next section. The model contribution from subgrid-scale and the resolved transports (Fig. 7c) tend to heat and cool the boundary layer and the area just above, respectively. In general, the contributions from this term are relatively small. As expected, the radiative term (Fig. 7d) exhibits a diurnal cycle with variations primarily introduced by the interaction between longwave cooling and shortwave absorption in clear air during suppressed periods as suggested by Parsons et al. (2000). As with the large-scale advection, some vertical structure is noted in regions of temperature inversions during this period. The diabatic term (i.e., the temperature change from latent heating and cooling associated with phase changes; Fig. 7e) is largely positive and limited to the lower levels of the atmosphere until the last day of the simulation. The primary exception to this point is the weak cooling that is observed within the boundary layer due to the evaporation of rainfall. The

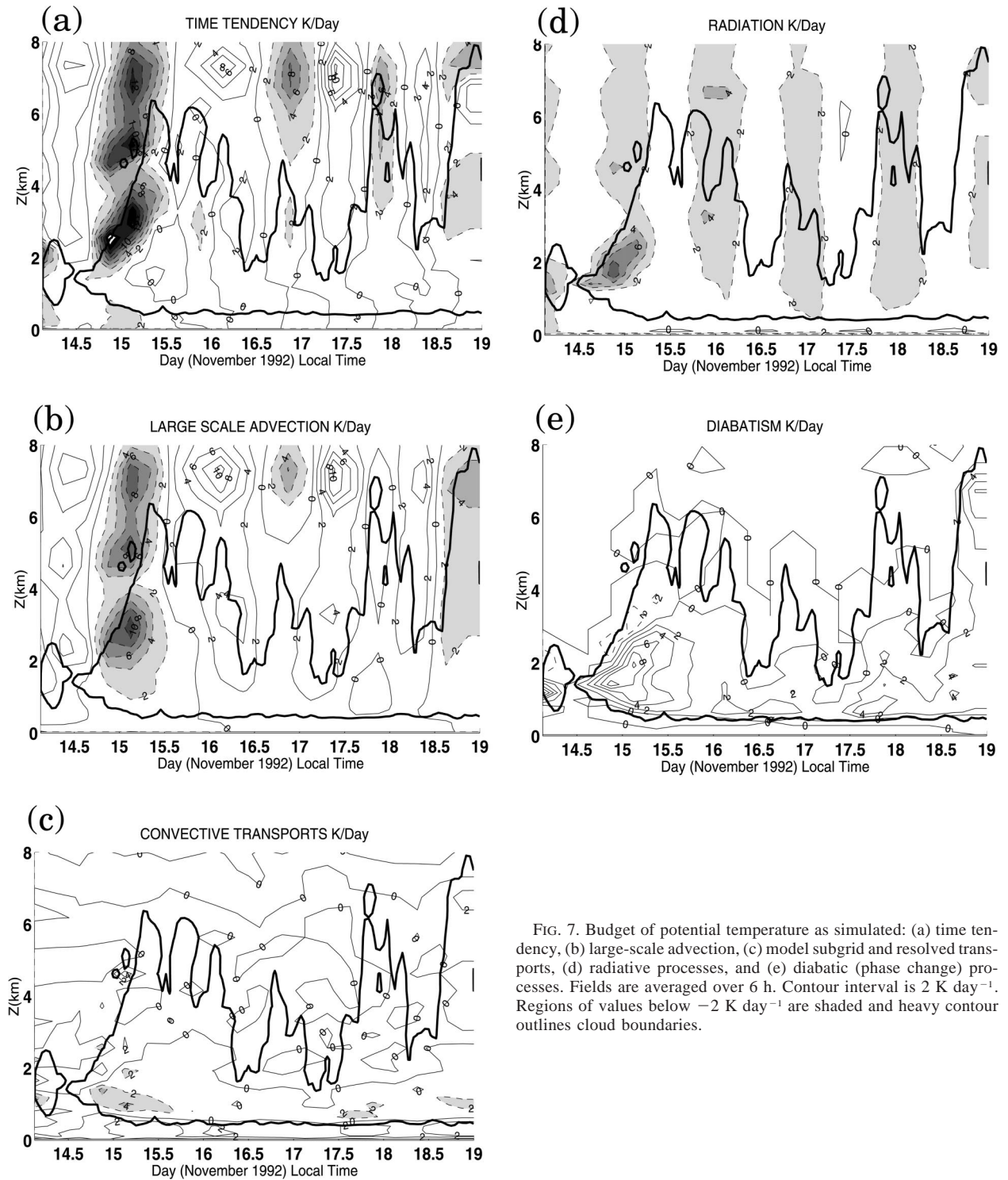


FIG. 7. Budget of potential temperature as simulated: (a) time tendency, (b) large-scale advection, (c) model subgrid and resolved transports, (d) radiative processes, and (e) diabatic (phase change) processes. Fields are averaged over 6 h. Contour interval is  $2 \text{ K day}^{-1}$ . Regions of values below  $-2 \text{ K day}^{-1}$  are shaded and heavy contour outlines cloud boundaries.

shallow nature of the clouds generally precludes the presence of a pronounced melting level. The radiative contribution, and to a lesser extent, the diabatic term explain most of temperature evolution between 1.5 and 4 km during the night. The diurnal signal from the diabatic term is difficult to detect. Thus the strong diurnal cycle above the

PBL is mainly due to diurnal variations in the large-scale vertical velocity and radiative processes, and does not seem related to diurnal variation of surface fluxes (related to those of SST) and associated vertical transports.

The moisture evolution can be studied in decomposing the time tendency of water vapor (Fig. 8a) as the

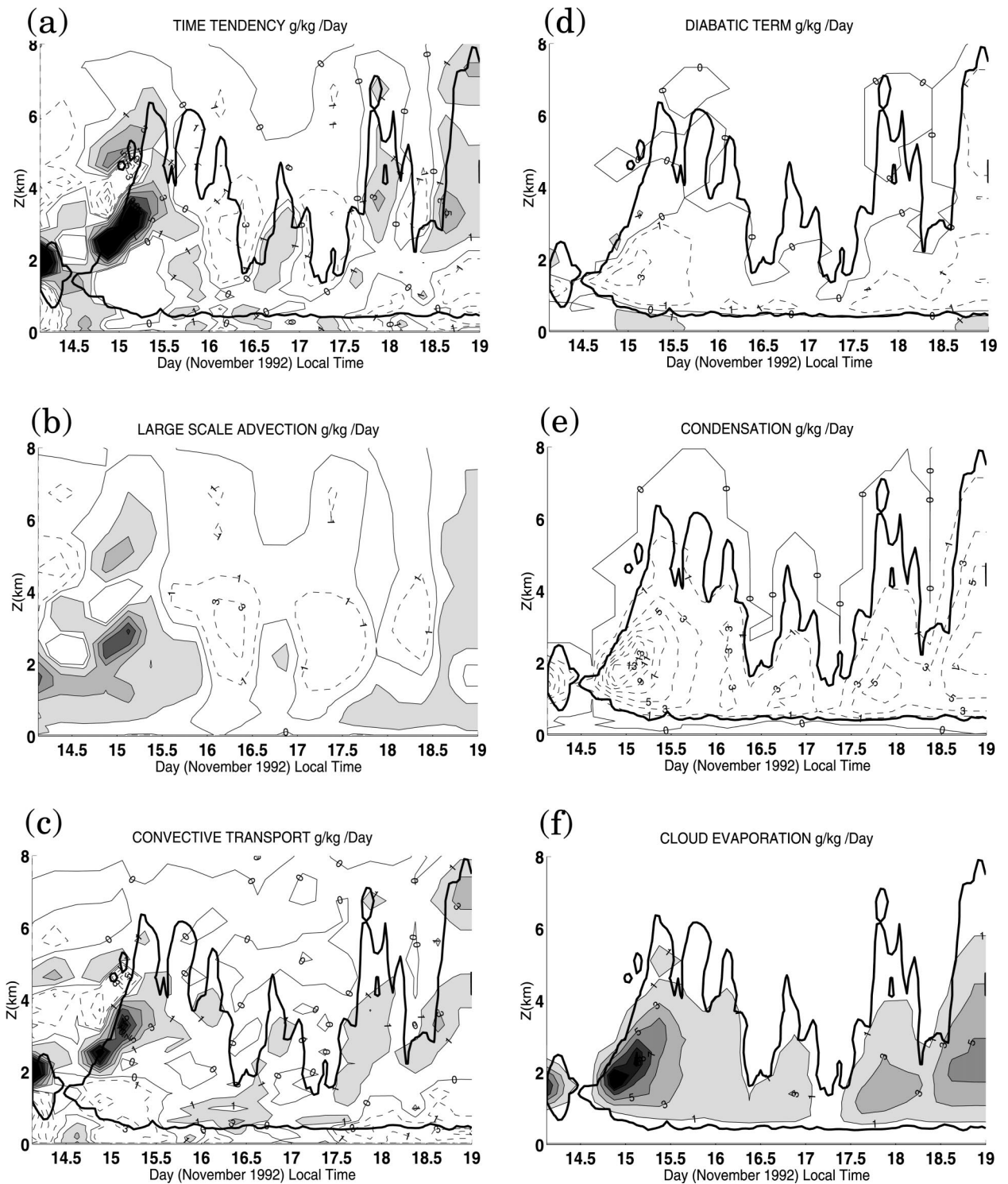


FIG. 8. Budget of specific humidity as simulated: (a) time tendency, (b) large-scale advection, (c) model subgrid and resolved transports, (d) net diabatic effect (phase change), (e) liquid condensation, and (f) cloud evaporation. Fields are averaged over 6 h. Contour interval is  $1 \text{ g kg}^{-1} \text{ day}^{-1}$ . Regions of values above  $1 \text{ g kg}^{-1} \text{ day}^{-1}$  are shaded and the heavy contour outlines cloud boundaries.

sum of the large-scale forcing (Fig. 8b), the sum of resolved and subgrid transports (Fig. 8c), and the net diabatic effect (Fig. 8e):

$$\frac{\partial q}{\partial t} = \left( \frac{\partial q}{\partial t} \right)_{\text{LS}} + \left( \frac{\partial q}{\partial t} \right)_{\text{Resolved Transport}} + \left( \frac{\partial q}{\partial t} \right)_{\text{Subgrid Transport}} + \left( \frac{q}{\partial t} \right)_{\text{Diabatic}}. \quad (2)$$

In many respects, the processes impacting the recovery of the moisture field (Eq. (2) and shown in Fig. 8) contrasts with the terms driving the changes in potential temperature (Fig. 7). One important aspect is that the largest time changes for the moisture field (Fig. 8a) took place below  $\sim 4\text{--}5$  km in height, while the time evolution for the potential temperature (Fig. 7a) had very regular changes extending from the lowest 2–3 km up through the middle troposphere with the largest changes appearing generally above  $\sim 7\text{--}8$  km. A similar statement could be made concerning differences in the patterns of large-scale advection for potential temperature (Fig. 7b) and water vapor (Fig. 8b) where large-scale advection in the potential temperature field occurs aloft. A striking feature of the water vapor budget is the strong evaporation rate (Fig. 8f) experienced by the clouds throughout this period, balancing an average of two-thirds of the condensation rate (Fig. 8e). The general diabatic effect is thus to decrease the water vapor content at a given level (Fig. 8d). This result is, of course, partly due to the water vapor convective transport (Fig. 8c). Vapor is indeed carried upward in convective clouds and condenses at higher levels in the atmosphere. The transports by model-resolved and subgrid-scale motions (Fig. 8c) explain a larger part of this transport, whereas the large-scale advection is secondary in contrast to the budget of potential temperature. For the large-scale and convective transports, the vertical patterning typically represents the vertical gradient of moisture.

In terms of the recovery in the water vapor in the model (Fig. 5) and the erosion of the very dry layer between 2 and 3 km (Fig. 1), the largest impact is from the convective transports (Fig. 8c). During the first 12 h of the simulation, the moistening of the atmosphere by convective transports peaks just above 2 km coinciding with shallow clouds. Subsequently, on 15 November the major changes in moisture distribution are observed between 2 and 4 km due to convective transports (Fig. 8c), when first individual shallow cloud tops reach up to 5–6 km (Fig. 6). When deeper convection begins to develop near the end of the simulation, the convective transports again moisten the cloud-containing layers resulting in an erosion of the relatively dry layer above  $\sim 5$  km (see Fig. 1). During these times of moistening of the dry air layer within the simulation, the large-scale forcing (Fig. 8b) also contributes to the moistening (Fig. 8a), although the convective transports are able to extend the moistening to higher elevations.

At other times, the large-scale advective term tends to dry the atmosphere.

The previous discussion seems to implicate the role of clouds in the atmospheric recovery. In order to quantify the role of clouds in atmosphere remoistening, the various contributions to the moisture budget have been averaged over a vertical layer representative of the upper cloud layer defined as the layer of 3-km depth beneath the cloud top. The same vertical layer for cloudy and noncloudy regions are used to integrate the different tendencies. These tendencies have been horizontally averaged over three different areas: total simulation domain (Fig. 9a), cloudy columns (Fig. 9b), and cloud-free columns (Fig. 9c). Cloudy columns are simply vertical columns that contain clouds (sum of liquid and solid water contents greater than  $10^{-3}$  g kg $^{-1}$  in at least one grid point). The tendencies from the cloudy and cloud-free columns have been weighted by the occupation rate of each defined region in order to obtain their respective contributions (Figs. 9b and 9c) to the total simulation tendency plotted in Fig. 9a. The averages of these three quantities are also given in Table 1 for the upper cloud layer for the period from 1800 LST 14 November to 0000 LST 19 November.

Confirming the discussion of Fig. 8, the convective transports and imposed large-scale advection are the largest contributions to the moistening over the total domain scale (Fig. 9a), although on average the convective transport is dominant (Table 1). In cloudy regions (Fig. 9b), the convective transport is the main process leading to the moistening, except prior to 1200 LST 15 November, when the large-scale advection and diabatic terms are significant. The convective transport of moisture in clouds represents a major contribution to the time tendency averaged on the full domain (Fig. 9a). The diabatic contribution over the entire domain is always negative as a consequence of the strong condensation (Fig. 9b and Table 1). In contrast, cloud-free regions (Fig. 9c) have experienced strong evaporation in the upper cloud levels. The convective transport in cloud-free regions (Fig. 9c) is important, but generally smaller than in cloudy regions.

From the summary shown in Table 1, where the convective transports are divided into vertical and horizontal advective terms, it is evident that the largest term for cloudy and cloud-free regions inside the vertical layer within 3 km of cloud top is the horizontal advection of moisture from moist to dry areas. Since in this modeling framework, the primary cause of horizontal gradients is cumulus convection and we are near cloud top, we interpret the horizontal advection term as the general detrainment that arises from the repeated penetrations of isolated convection into drier layers. In contrast, the vertical advection is primarily drying, even in cloudy regions. This is a consequence of the fact that only a small fraction of the cloudy column actually contains convective cores with strong updrafts and the budget is near cloud top. This result is supported in the

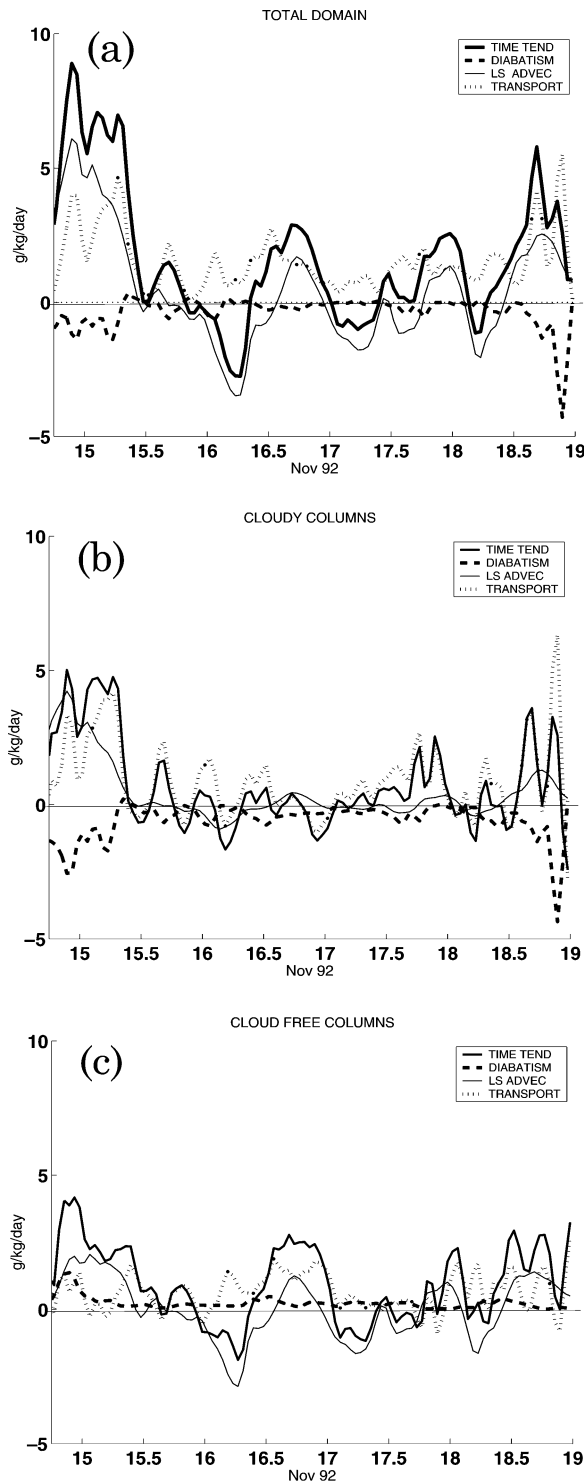


FIG. 9. Time series of simulated vapor budgets ( $\text{g kg}^{-1} \text{day}^{-1}$ ) as averaged through the upper layer of 3 km from the mean cloud top for (a) total model domain, (b) cloudy region, and (c) cloud-free region. Fields are 3-h running averages.

TABLE 1. Vapor budgets ( $\text{g kg}^{-1} \text{day}^{-1}$ ) as averaged from 1800 LST 14 Nov to 0000 LST 19 Nov and through the upper layer of 3 km from the mean cloud top for contributions from: the total model domain, the cloudy region, and the cloud-free region.

Vapor budget terms	Total	Cloudy	Cloud-free
Time tendency	1.67	0.72	0.95
Diabatic term	-0.36	-0.59	0.23
Vertical advection	-1.90	-1.00	-0.90
Horizontal advection	3.44	1.88	1.56
Total advection	1.54	0.88	0.66
Large-scale advection	0.49	0.43	0.06

time series of the horizontal, vertical and total advection (Fig. 10). Consistently, the general impact of clouds is to moisten by horizontal advective processes representing detrainment and mixing at the lateral edges of the cloud as the vertical transport is always smaller in the upper part of clouds (except during the three last hours, when deep convection occurs). Another surprising point from these budgets (see Table 1) is that the large-scale advection is moistening the environment and that the term for the cloudy region is larger than for the cloud-free regions. Examination of the time series of this term for the cloudy and cloud-free environments (Figs. 9b and 9c) shows that the explanation for this difference is that clouds tend to form much more in the presence of favorable large-scale advection, while cloud-free regions experience both positive and negative large-scale advection that results in a far smaller average.

Looking at the results thus far, one point of view is that the moistening occurs when convection in the model occurs in the presence of favorable large-scale advection. To illustrate the sensitivity to external parameters, several numerical experiments have been performed and are briefly presented here through a depiction of the time evolution of rainfall (Fig. 11). When the large-scale advection is neglected, the rainfall stays very small (below  $2.5 \text{ mm day}^{-1}$ ), except during the last day. In this experiment, the recovery was slower and the instability was not released by more significant convective events leading up to the deep convection at the end of the period, but instead was allowed to continue to build. This result shows that, despite the strong link between the large-scale advection and convection dictated by the large Rossby radii of deformation in the Tropics, deep convection can still occur with no imposed large-scale advection when the cloud fraction is low. In contrast, the rain amount is only slightly changed when the SST is held or when using the complete large-scale advection dataset provided by Ciesielski et al. (1997) (see section 2). However, the timing and the intensity of the latter deep convective event are different, especially when the SST is kept constant (related to smaller surface sensible and latent heat fluxes). The results appear weakly sensitive to the choice of large-scale vertical advection in terms of rainfall for shallow isolated convection.

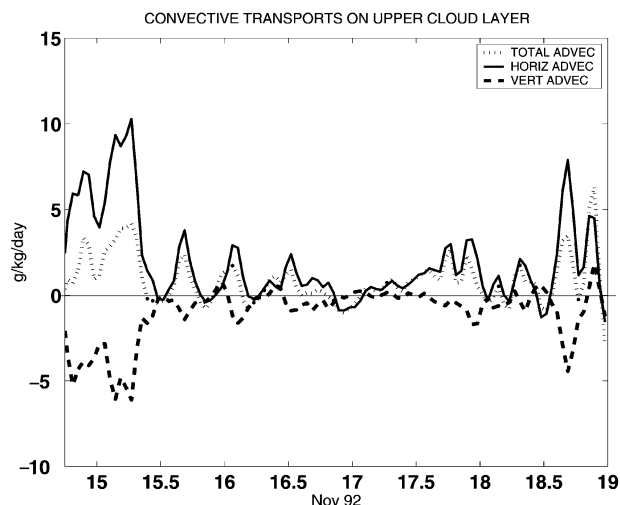


FIG. 10. Same as Fig. 9a (total model domain), except for the model transport and its vertical and horizontal components.

### 5. What processes limit cloud-top heights?

Several studies have suggested that the moisture above the boundary layer plays a large role in regulating the convective cloud development in the Tropics through entrainment/detrainment processes (e.g., Raymond 1995; Brown and Zhang 1997; Sherwood 1999). The importance of entrainment and detrainment processes in describing the observed general characteristics of TOGA COARE clouds can be found in Zuidema (1998) and Wei et al. (1998). Zuidema (1998) used a simple buoyancy sorting model to show that when water loading and mixing were included, significant detrainment took place in the stable layers leading to a minimum in cloudiness between  $\sim 800$  and  $600$  hPa. On the other hand, analysis of radar echo tops observed during TOGA COARE showed a well-marked trimodal distribution termed as shallow cumulus, congestus, and cumulonimbus (Johnson et al. 1999). The authors related these different cloud-top heights to the presence of several prominent stable layers at  $\sim 2$ ,  $5$ , and  $15$  km. Additional discussions on the role of stable and dry layers in controlling cloud heights can be also be found in Mapes and Zuidema (1996) and Parsons et al. (2000). While these results indicate that mixing and interactions with stable layers are important factors in describing TOGA COARE clouds, we are clearly far from a quantitative characterization of convection development as a function of environmental parameters. One reason is the experimental difficulties in simultaneously observing the complete temporal evolution of individual clouds and their close environment. Analysis of the present simulation, with convection taking place in a large-scale environment that changes dramatically, is presented herein as a first step in this characterization. As previously described, the period exhibits various changes in cloud top heights in response to these environmental changes. Thus the present simulation seems to be an

appropriate to identify those factors that limit the height of cloud top.

Convective available potential energy (CAPE) is a basic integral quantity, which can be tentatively related to the convection development. The data plotted in Fig. 12a shows that there is no obvious dependence of cloud-top heights on CAPE. For example, values of CAPE ranging from  $500$  to  $1500$   $\text{J kg}^{-1}$  lead to virtually the same cloud-top height. This result is in agreement with previous observational studies (Mapes and Houze 1992; Alexander and Young 1992). Using a multivariate analysis of sounding and satellite data, Sherwood (1999) also suggested that a minimum CAPE of  $100$ – $300$   $\text{J kg}^{-1}$  is required for convection but there was no indication that further increases could lead to a larger probability of convective activity.

A second parameter, sometimes invoked to explain the limitation of vertical convective development, is humidity decreasing above the cloud top. The relationship between the environmental relative humidity in the model and the simulated cloud tops is shown in Fig. 13. Only a weak relationship appears between the relative humidity and the cloud top in the simulation, as cloud tops are rarely observed very far above the  $\sim 30\%$  relative humidity contour. If a strict dependency existed between cloud top and the relative humidity, one might expect dependence of cloud top on the relative humidity just above the clouds, as if the clouds were unable to penetrate and exist in an environment where the relative humidity is below a certain value. The relationship between cloud-top height and relative humidity just above the cloud top (Fig. 12b) does not show such a simple dependency. For example, cloud tops at  $\sim 2$ -km altitude can occur when the relative humidity above the clouds ranges from  $10\%$  to  $65\%$ . The general decrease of humidity viewed on this plot depicts its usual decrease with the altitude. Cloud-top detrainment alone cannot thus explain the limited vertical extent of clouds.

We next looked at how dry air present above the boundary layer contributes to limit the vertical development of convective clouds through, say, buoyant parcels mixing with their environment as the parcel ascends. To this end, the difference between the mean saturated specific humidity and the mean specific humidity has been computed at each altitude. This quantity is a crude representation of dry air entrainment and will be referenced hereafter as the vapor deficit. To crudely represent mixing one must assume that the entrainment at each level is proportional to the difference of saturated moist static energy and moist static energy. A time series of the vapor deficit is shown in Fig. 14. A very strong deficit is present on 14 November at the upper levels of clouds and above. After this date, two less intense deficit layers are observed around  $3$ – $4$  and  $7$ – $8$  km and exhibit time evolution of their amplitudes. Between 0600 LST 16 November to 1800 LST 18 November (except for small periods), these layers are roughly located at the upper layers of clouds and above. On 15 November, the clouds

## SURFACE RAINFALL

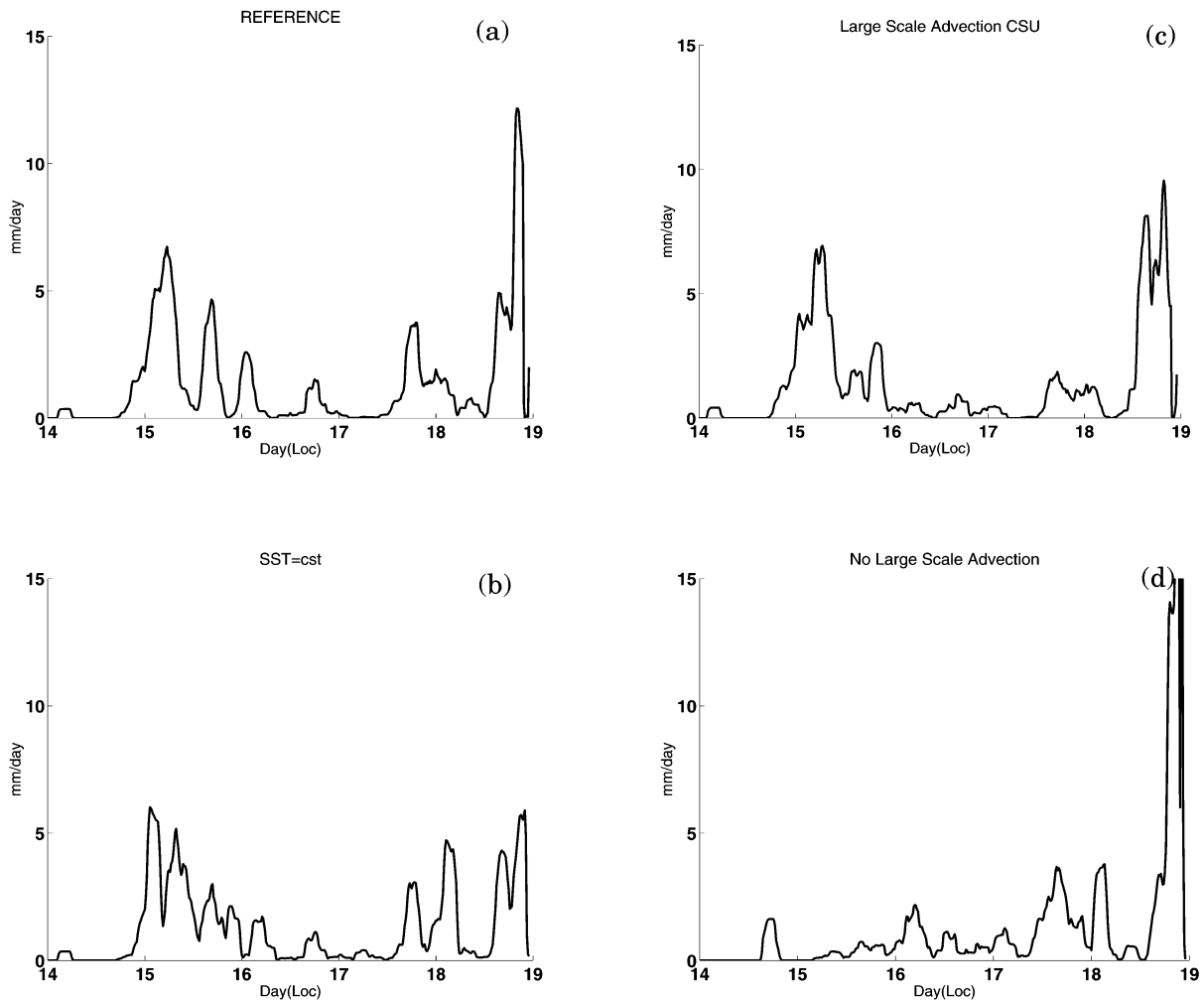


FIG. 11. Comparisons of rainfall ( $\text{mm h}^{-1}$ ) from different numerical sensitivity experiments: (a) reference, (b) SST constant, (c) full large-scale advectations from CSU, and (d) no large-scale advectations.

periodically go through the deficit layer, which has a small vertical extent as well as weak amplitude. Nevertheless, the cloud top does not exceed 6 km on this day. To begin to quantify this relationship, a time series of the cloud-top height and the vapor deficit vertically integrated between 2 and 6 km is shown in Fig. 15. The two quantities have a general tendency to be clearly of opposite phase. Consistent with the discussion in the previous section, cloud-top height maxima occur about 3 hours later than the vapor deficit minima after 16 November. The diurnal variation of vapor deficit observed after 16 November can be related to those of the moisture tendency (Fig. 8) and horizontal advection terms (Fig. 10) described in the previous section. For example, it was shown that the diurnal variation of the large-scale velocity was the cause of these variations in the moisture

field and that clouds moisten the environment through general detrainment and mixing.

In order to analyze more quantitatively the potential for dry air entrainment, relationships between the cloud-top height and vertically averaged vapor deficit are plotted in Fig. 16 for characteristic periods and layers selected from Fig. 14. For 14 November, just after the intense dry intrusion, a linear relationship is obtained (Fig. 16a), showing how the cloud top is gradually increasing in conjunction with the decrease of vapor deficit averaged between 1.4 and 3 km. The cloud-top heights on Fig. 16b exhibit also a strong dependency on vapor deficit averaged on 2.5–4.5-km layer but for deficit values smaller than  $\sim 3 \text{ g kg}^{-1}$ , cloud-top heights vary from 3.8 to 13 km. Thus as environments moisten, the vertical development of the clouds become far less

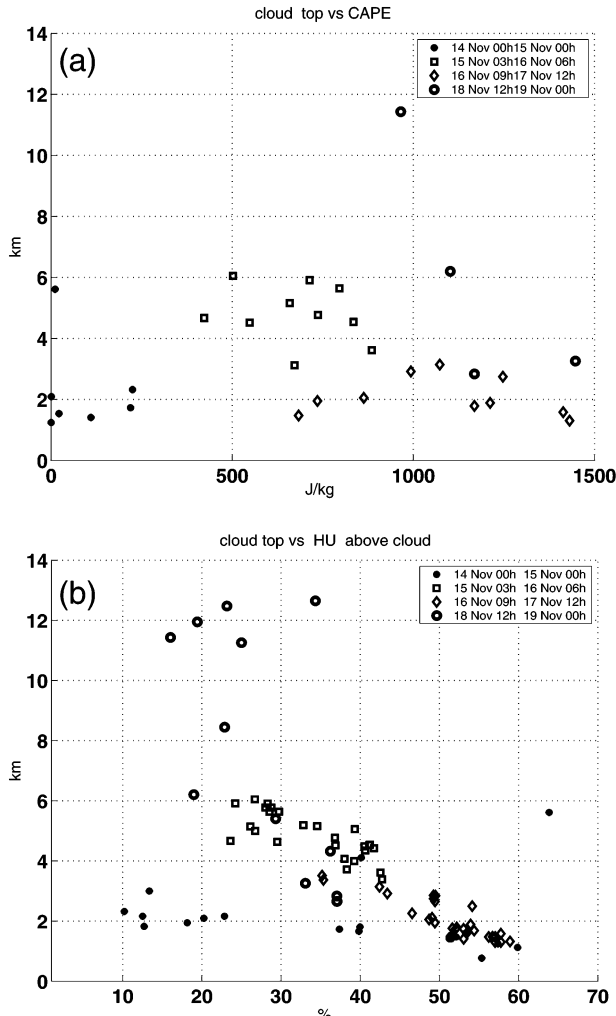


FIG. 12. Mean cloud-top heights as a function of (a) CAPE and (b) relative humidity above clouds, computed as the average on the two first model levels located above mean cloud top. Fields are 3-h running averages.

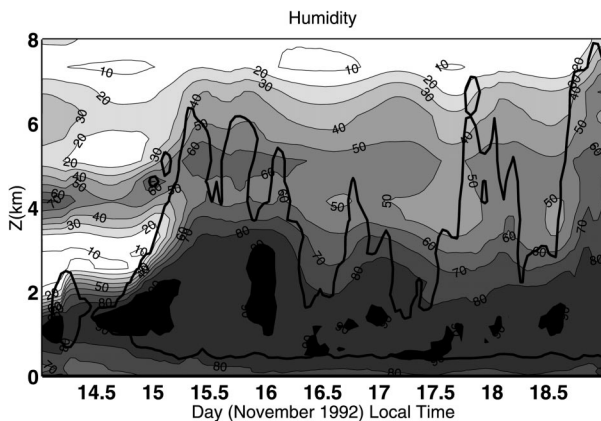


FIG. 13. Time-height cross section of simulated relative humidity. Heavy contour outlines cloud boundaries.

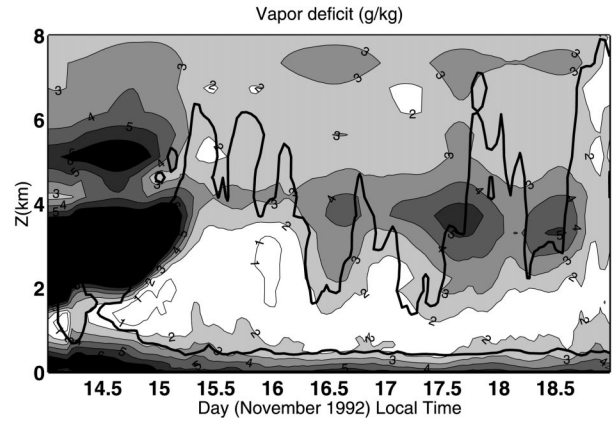


FIG. 14. Time-height cross section of simulated vapor deficit (interval  $1 \text{ g kg}^{-1}$ ) defined at each level as the difference between the mean saturated and specific humidity. Black regions correspond to values above  $6 \text{ g kg}^{-1}$ . Heavy contour outlines cloud boundaries.

dependent on variations in the magnitude of the vapor deficit and thus on entrainment.

Another factor playing a role in limiting the vertical extent of clouds is the mean vertical stratification, which is shown for the period of interest in Fig. 17. Since there is not much difference between the potential temperature and virtual potential temperature, the vertical derivative of the potential temperature is used in Fig. 17 to depict the stability allowing a direct thermal complement to the moisture fields presented earlier. Different inversions are observed with intensities varying as a function of time. At the beginning of the simulation period, enhanced stability exists at 1.75, 4.5, and 7.2 km. The lowest stable layer is very large (around  $12 \text{ K km}^{-1}$ ) and appears at the base of the high vapor deficits shown earlier in Fig. 14. The relationship between the

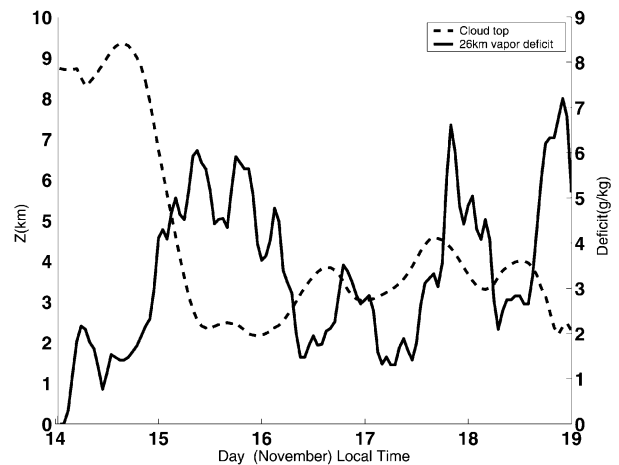


FIG. 15. Time series of mean cloud-top heights (km) and vapor deficit ( $\text{g kg}^{-1}$ ) as diagnosed from the reference experiment. The vapor deficit is defined at each level as the difference between mean saturated and specific humidity and is vertically averaged between 2 and 6 km. Fields of vapor deficit and cloud-top height are averaged over 1 and 3 h, respectively.

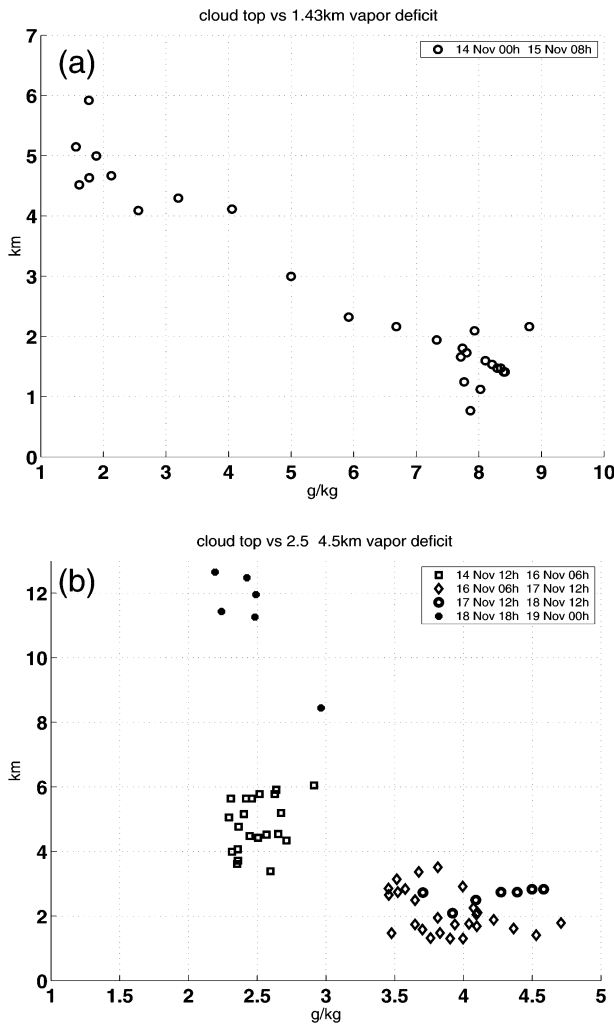


FIG. 16. Mean cloud-top heights (km) for selected periods as a function of humidity deficit ( $\text{g kg}^{-1}$ ), averaged (a) between 1.4 and 3 km, and (b) between 2.5 and 4.5 km. Note the difference of the axes between (a) and (b). Fields are 3-h running averages.

thermal field and the dry air, driven in part by clear air radiative processes, was first noted and explained by Mapes and Zuidema (1996) and is enough to explain the limited extent of clouds. During this period, given the large magnitude of the thermal stability and the vapor deficit, it is not surprising that convective development is limited to the base of the dry air mass. After the first day of the simulation period, the strongest thermal stability is located at  $\sim 7$  km in height with other layers located at  $\sim 3$  and 5 km in height. The strong thermal stability at  $\sim 7$  km tends to strengthen with time coinciding with a dry layer above the inversion that becomes evident late in the day on 15 November. The relationship between the dry air and the thermal inversions is also evident in the inversion near 5 km in height as this inversion weakens following the moistening of the layer immediately above the inversion. The cloud-top heights generally coincide close to the layers of

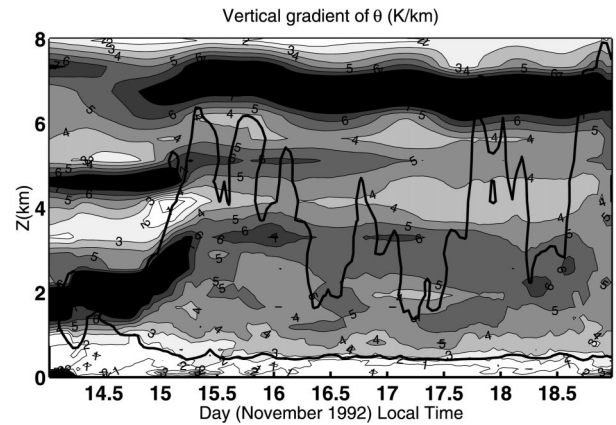


FIG. 17. Time–height cross section of vertical gradient of  $\theta$  (interval  $1 \text{ K km}^{-1}$ ) as simulated by the CRM. Black regions correspond to values above  $7 \text{ K km}^{-1}$ . Heavy contour outlines cloud boundaries.

enhanced stability. When the cloud tops are able to penetrate these strong inversions, such as late in the day on 14 and 18 November, the convection in these low cloud fraction situations corresponds to favorable large-scale forcing.

The observed sounding on 2300 LST 15 November is shown in Fig. 18. Two main dry layers are observed between 2–3.5 and 5–7 km with thin dry layers also apparent near  $\sim 4$  km. At the base of each of the two main layers, temperature inversions occur as expected from the radiative effects discussed earlier. In general, in the model and observations, the layers of enhanced stability in the potential temperature, as expected, coincided with these temperature inversions. A smaller inversion is observed at the middle of the thin dry layer around 4 km. When convection reaches any inversion, the buoyancy is sharply decreased and can even become negative. A large amount of mass can then be detrained.

Thus, both vapor deficits and stratification anomalies are generally present together. The magnitude and depth of these anomalies are important to consider in explaining the variations in cloud-top heights observed during this period. Sometimes one process is enough to explain the cloud-top height, while for others a combination of

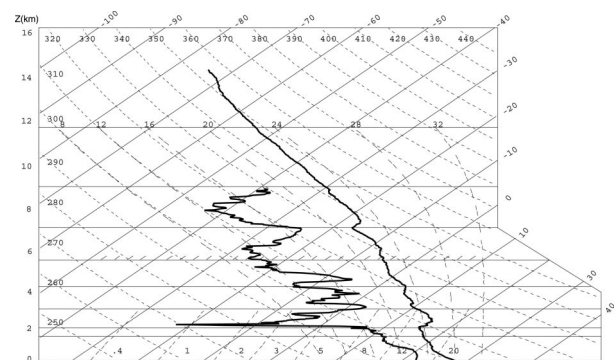


FIG. 18. Sounding from R/V *Moana Wave* at 2300 LST 15 Nov.

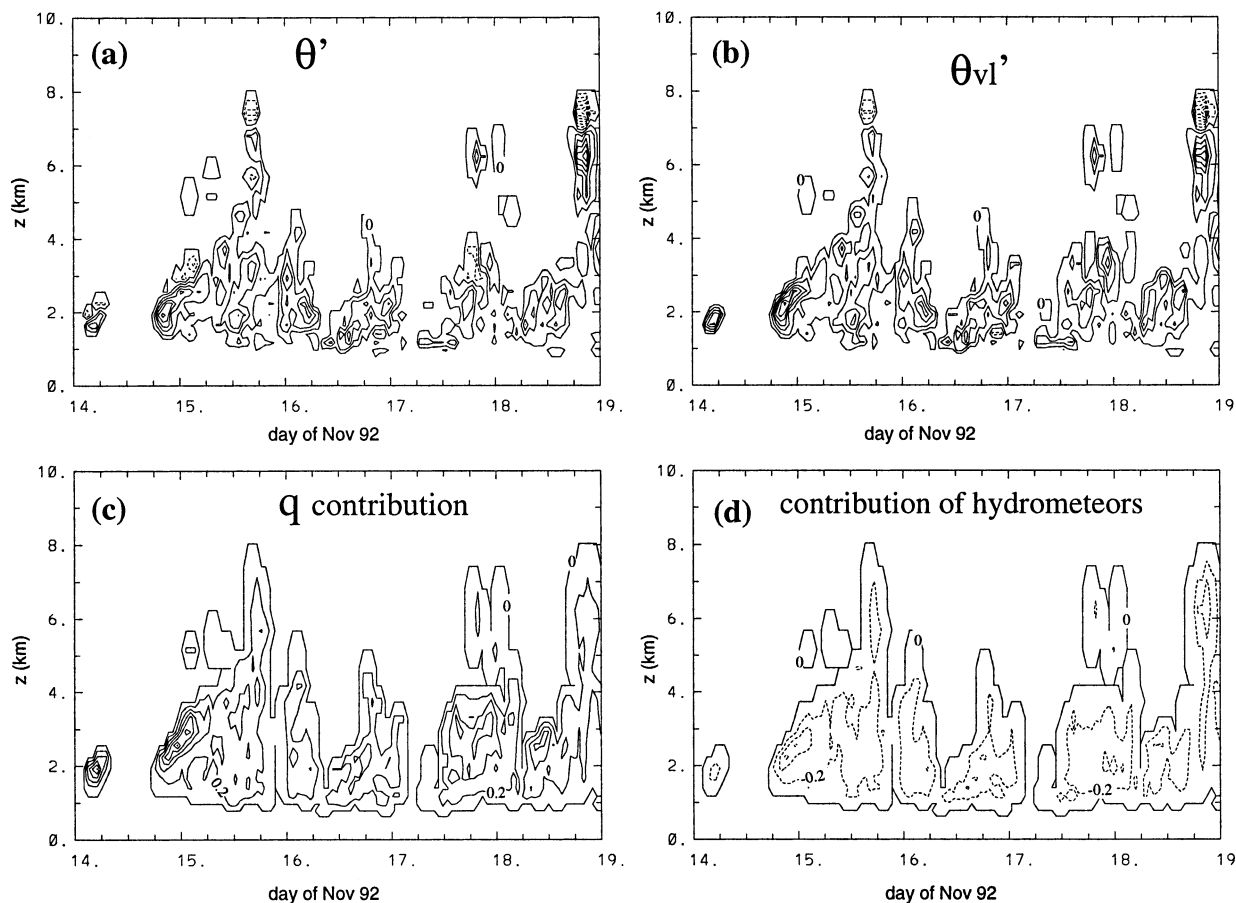


FIG. 19. Time–height cross section of the simulated buoyancy in convective cores ( $w > 1 \text{ m s}^{-1}$ ): (a) total, (b) temperature contribution, (c) vapor contribution, and (d) water loading. The buoyancy is plotted after multiplying by a factor  $\theta_v/g$  (interval of 0.2 K) and are 3-h running averages. The first solid line corresponds with a zero buoyancy.

two processes needs to be advocated, such as for the period 1700 LST 16 November to 1800 LST 17 November. These features can be analyzed in the context of buoyancy. Since the Global Atmospheric Research Program (GARP) Atlantic Tropical Experiment (GATE), it is known that convective updrafts over tropical oceans are weaker than those over continents. Analysis of data from oceanic experiments GATE, Equatorial Mesoscale Experiment (EMEX), Taiwan Area Mesoscale Experiment (TAMEX), and TOGA COARE (Zipser and LeMone 1980; Jorgensen et al. 1985; Jorgensen and LeMone 1989; Lucas et al. 1994; Wei et al. 1998) have also shown that the measured updraft velocities are much smaller than that predicted by parcel theory. Moreover, observational (Lucas et al. 1994; Wei et al. 1998) and modeling (Guichard et al. 1997) papers have indicated that cloud buoyancy is small on average (few tenths of degree Kelvin). Only strong updrafts (velocities larger than  $5\text{--}7 \text{ m s}^{-1}$ ) exhibit buoyancy larger than 1 K. It was suggested that water loading and entrainment largely contributed to reduce the buoyancy in convective updrafts over tropical oceans. Guichard et al. (1997) suggested also that in the Tropics, where the Rossby

radius is large, any cloud buoyancy excess is rapidly dispersed by gravity waves. These features can explain the strong sensitivity of cloud development to dry layers and inversions found in the present study. Any small reduction of buoyancy in convective updrafts can lead to neutral or negative buoyancy.

A future paper will be largely dedicated to the detailed analysis of simulated buoyancy. However, the general characteristics of the cloud buoyancy are illustrated in Fig. 19. In this figure, hourly averages of the buoyancy and its components within convective cores (vertical velocities in excess of  $1 \text{ m s}^{-1}$ ) are presented. Several conclusions can be reached from examination of this time series. First, the contributions of the potential temperature fluctuations (Fig. 19b) to the total buoyancy (Fig. 19a) are generally on the order of 1 K. In contrast, undiluted parcels should have maximum thermal buoyancies of several degrees or more. Second, the negative buoyancy from hydrometeors (Fig. 19d) is generally quite small and typically only a few tenths of a degree Kelvin. These results are quite similar to the observations of Wei et al. (1998) that indicated convective cores observed during TOGA COARE generally tend to have

thermal buoyancies well below those of an undiluted parcel due to mixing with the environment, but that parcels do not maintain the water loading to a significant degree.

In our analysis, we also show the contribution to the parcel buoyancy from water vapor (Fig. 19c). At times these contributions exceed 1 K and thus approach the thermal contribution. These occur when the parcels with water vapor contents, which are more characteristic of the boundary layer (15–20 g kg<sup>-1</sup>), are penetrating the extremely dry layers associated with the dry intrusion with mixing ratios of only a few grams per kilogram. In general, the parcels in this situation begin their ascent as thermally buoyant and eventually become buoyant in greater part due to an excess of water vapor. This term allows for increased penetration of convection into the dry layer where detrainment and thus moistening can occur. This positive effect occurs mainly on 14 November and explains why some clouds reach levels higher than the dry air layer. While previous studies and indeed the bulk of this paper stress that the dry air inhibits convection through forming thermal inversions and through the negative impacts of entrainment, this figure shows that the dry air can actually significantly increase the positive buoyancy of clouds. Since the dry air is associated with a general reduction in cloud-top height in both the observations and the simulations, the negative impact of the dry air is dominant for COARE clouds. In actuality, the degree to which the positive or negative impacts of the presence of dry air dominates depends on the inversion strength and on the amount of mixing between the parcel and its environment. To accurately predict cloud tops for these types of regimes with a numerical model, two features should be carefully examined. Firstly, the vertical gradients of moisture must be well represented since these gradients drive the clear-air radiative processes responsible for the formation and/or maintenance of the inversion. Secondly, the large amount of mixing needs to be correctly parameterized.

## 6. Conclusions and discussion

This study investigated the recovery of the lower and middle troposphere to moist conditions, and the factors that limit cloud-top heights, following the arrival of a dry intrusion during TOGA COARE through the use of a cloud-resolving model. This dry air arrived on 12 November 1992 and the recovery of these layers lasted until 19 November. During this recovery period, the moisture and temperature fields evolved differently. The large-scale forcing and radiation explain most of the potential temperature time evolution, whereas convective transports are more important for the moisture time evolution. This difference is expected given that the thermal differences between the convective parcel and the environment have been shown to be small, while the moisture differences can be quite large. In addition,

with the large Rossby radius a rapid adjustment should occur as a result of any thermal differences created by convection. A strong diurnal cycle of temperature above the PBL is observed due to large-scale velocity and radiative processes, but not to diurnal variation of surface fluxes (related to those of SST) and related vertical transports. Due to marked morning large-scale subsidence, diurnal variations of temperature were observed from 16 November; while during earlier times, the variation and the period are larger. The radiation also exhibits a diurnal cycle with strong local maxima at midnight in the region of dry air as suggested by Parsons et al. (2000). This radiative effect contributes to maintaining the temperature inversion through most of the period.

On 14 November, the remoistening is due to the moisture convective transport from boundary layer into the first dry air layer. Very shallow clouds are present even though condensation and evaporation rates are almost equivalent due to the presence of extremely dry air. After 15 November, individual shallow clouds extend to 5–6 km and are the main cause of moistening through their convective transports. After 16 November, moistening mainly occurs during the afternoons and evenings due to transports induced by shallow and deep convective clouds. In contrast, during the mornings the moisture decreases due to the large-scale advection, except in the boundary layer. The remoistening of the secondary dry layer (above 5 km) gradually occurs, resulting from isolated deep convective cells. A striking feature is the strong evaporation rate experienced by the clouds throughout the whole period, balancing, on average, two-thirds of the condensation rate. The horizontal advection associated with convective transport occurring in the upper cloud layer is the major cause of the gradual moistening of the atmosphere. This point has been hypothesized in various observational studies. The remoistening is thus the main result of detrainment of cloud air in the environment occurring on the lateral edges of upper cloudy layers. In this process, shallow convective clouds are crucial and present during the entire period.

As found in Parsons et al. (2000), at the beginning of the period, large values of convective inhibition prevented the convection triggering. After 1200 LST 15 November, the CIN impact slows down the cloud development rather than prevents it. When clouds are present, their tops generally reach only intermediate levels of troposphere (between 4 and 6 km), well below the tropopause (around 15 km). This feature is consistent with available radar and profiler observations. Cumulus congestus thus represents the major mode of convection through the considered period, except during the end of the period where isolated deep convective cells are able to develop.

The second part of the study concentrated on extricating the factors limiting the observed cloud-top height. Two negative effects of the dry layers inhibiting

the vertical development of clouds were the direct effect through cloud detrainment and an indirect effect through the strong inversion created by radiative processes at the base of the dry layers. Entrainment leads to a reduction in buoyancy making the inversions more important in controlling the cloud top. Thus both effects are necessary to explain the general evolution of cloud tops, although for some periods one is sufficient to explain the simulated cloud-top height. To quantify the direct effect (dry air entrainment), the difference between the mean saturated specific humidity and the mean specific humidity at each altitude was found to be a useful quantity. Using this quantity, the dry air entrainment is assumed to be proportional to the difference of saturation moist static energy and moist static energy. The intensity of this quantity and its vertical extent are two important factors explaining many differences of cloud-top heights for different stages of a dry layer. There is one positive impact of the dry air on convection. When shallow clouds first penetrated into the dry layer significant parcel buoyancy was generated by excess water vapor aiding the penetration of the cloud into the dry layer. While the general evolution of the recovery process is consistent with the conceptual model of Parsons et al. (2000), this finding was not part of the conceptual model.

The strong sensitivity to the temperature inversions found in the present study is explained by the small buoyancy found in the clouds especially outside the convective cores. Any small reduction of buoyancy in convective updrafts (i.e., entrainment of dry air) is thus able to lead to neutral or negative buoyancy. This result is consistent with the analysis of moistening processes showing that the horizontal convective transport is the major process moistening the atmosphere in the analyzed period. The study thus emphasizes that the buoyancy deduced from the pseudo-adiabatic motion of a parcel is not enough to determine the cloud-top height. Treating convection as a reversible adiabatic process, where condensed water is carried vertically with the rising parcels, is also not a valid concept for these types of clouds, since the water content is small. This result is in agreement with the previously cited paper but stands in contrast to the findings of Carpenter et al. (1998) where reversible processes were found to provide a framework for discussing congestus evolution in simulations of congestus clouds over an isolated mountain range in middle latitudes. A subsequent paper will focus on that point by looking thoroughly at the simulated buoyancy distribution. In addition, less sensitivity of convective development to the presence of dry air can be expected for midlatitude cases where the buoyancy is generally larger (and so CAPE) than in the Tropics.

So far, dry air has been presented in this paper as inhibiting the convective development. As discussed in papers dealing with squall lines, the presence of a dry air layer can intensify the deep convection (e.g., Zipser 1977; Redelsperger and Lafore 1988). Indeed when con-

vection is able to develop elsewhere and propagate, the intensity of convection is increased in regions where a dry layer exists through the increase of downdraft evaporation. This evaporation then increases the intensity of the cold pool associated with the convective system. The convective downdrafts thus inject dry air in the boundary layer (e.g., Redelsperger and Lafore 1988; Raymond 1995). Squall lines observed during the West African monsoon are archetypes of such features, the dry air coming from the African deserts. Another potential case is the development of convection in the presence of very strong external forcing. Thus dry air can be a factor inhibiting or increasing the convection, depending on the convection stages, forcings, and intensity of triggering mechanisms. Present findings suggest also that statistical equilibrium as discussed by Emanuel et al. (1994) and Raymond (1995) probably needs to be reviewed; that is, a strict one-to-one relationship between boundary layer entropy and tropospheric temperature is not fully suitable and needs to be revisited in order to take into account the presence of dry intrusions (i.e., entrainment at each level of cloud dramatically changes the entropy of the parcel). First, a complete climatology of dry air intrusions is necessary to quantitatively address this fundamental issue. It is a difficult task in regard to our poor knowledge of global humidity fields.

All these results need to be carefully thought of in terms of the parameterized representation of convection in mesoscale and large-scale models. As a relatively large number of processes are found to be important for the analyzed period (radiation, shallow and deep convection, boundary layer transports), this period is a difficult but efficient testbed for models ranging from cloud-resolving models to general circulation models. The representation of moisture entrainment and shallow convection should be particularly examined. We feel that this testbed should also be considered as such mechanisms described in this paper are likely acting in less dramatic ways in numerous situations. For example, convective activation can be delayed by many hours by the presence of small dry air layers or weak inversions. In order to predict the proper onset of convection and consequently the correct diurnal cycle, careful consideration of model treatment of the processes investigated in the case is thus also necessary for these problems. Of course, correct treatment of entrainment and thus cloud tops is crucial for proper representation of water vapor transports and convective heating. Since the buoyancy is small, in part due to entrainment, relatively weak thermal inversions can limit cloud tops in nature. These inversions are, in turn, dependent on vertical variations in water vapor. If parameterizations of the clouds and convective transports within the model are to be based on the model representation of the large-scale flow, having the model correctly representing the inversions and moisture gradients will be a significant challenge.

**Acknowledgments.** The authors wish to thank the journal reviewers for their critical reviews, and Celia Darnel for helping us correct grammatical problems. We want also to thank Dick Johnson and Paul Ciesielski (CSU) for making available the large-scale forcing dataset and Tom Saxen (CSU) for providing a subset of radar data.

## REFERENCES

- Alexander, G., and G. S. Young, 1992: The relationship between EMEX mesoscale precipitation feature properties and their environmental characteristics. *Mon. Wea. Rev.*, **120**, 554–564.
- Balaji, V., and J.-L. Redelsperger, 1996: Sub-gridscale effects in mesoscale deep convection: initialisation, organization and turbulence. *Atmos. Res.*, **40**, 339–381.
- Brown, R. G., and C. Zhang, 1997: Variability of midtropospheric moisture and its effect on cloud-top height distribution during TOGA COARE. *J. Atmos. Sci.*, **54**, 2760–2774.
- Caniaux, G., J.-L. Redelsperger, and J.-P. Lafore, 1994: A numerical study of a stratiform region of a fast-moving squall line. Part I: General description and water and heat budgets. *J. Atmos. Sci.*, **51**, 2046–2074.
- Carpenter, R. L., Jr., K. K. Droegemeier, and A. M. Blyth 1998: Entrainment and detrainment in numerically simulated cumulus congestus clouds. Part I: General results. *J. Atmos. Sci.*, **55**, 3417–3432.
- Ciesielski, P. E., L. M. Harten, and R. H. Johnson, 1997: Impacts of merging profiler and rawinsonde winds on TOGA COARE analysis. *J. Atmos. Oceanic Technol.*, **14**, 1264–1279.
- DeMott, C. A., and S. A. Rutledge, 1998: The vertical structure of TOGA COARE convection: Part II: Modulating influences and implications for diabatic heating. *J. Atmos. Sci.*, **55**, 2748–2762.
- Emanuel, K. A., and M. Živković-Rothman, 1999: Development and evaluation of a convection scheme for use in climate models. *J. Atmos. Sci.*, **56**, 1766–1782.
- , J. D. Neelin, and C. S. Bretherton, 1994: On large-scale circulations in convecting atmospheres. *Quart. J. Roy. Meteor. Soc.*, **120**, 1111–1143.
- Grabowski, W. W., X. Wu, and M. W. Moncrieff, 1996: Cloud resolving modeling of tropical cloud systems during Phase III of GATE. Part I: Two-dimensional experiments. *J. Atmos. Sci.*, **53**, 3684–3709.
- , —, and —, 1998: Cloud resolving modeling of tropical cloud systems during Phase III of GATE. Part II: Effects of resolution and the third spatial dimension. *J. Atmos. Sci.*, **55**, 3264–3282.
- Guichard, F., J.-L. Redelsperger, and J.-L. Lafore, 1996: The behaviour of a cloud ensemble in response to external forcings. *Quart. J. Roy. Meteor. Soc.*, **122**, 1043–1073.
- , J.-P. Lafore, and J.-L. Redelsperger, 1997: Thermodynamical impact and internal structure of a tropical convective cloud system. *Quart. J. Roy. Meteor. Soc.*, **123**, 1043–1073.
- , J.-L. Redelsperger, and J.-P. Lafore, 2000: Cloud-resolving simulation activity during TOGA-COARE: Sensitivity to external sources of uncertainties. *Quart. J. Roy. Meteor. Soc.*, **126**, 3067–3095.
- Johnson, R. H., P. E. Ciesielski, and K. A. Hart, 1996: Tropical inversions near the 0°C level. *J. Atmos. Sci.*, **53**, 1838–1855.
- , T. M. Rickenbach, S. A. Rutledge, P. E. Ciesielki, and W. H. Schubert, 1999: Trimodal characteristics of tropical convection. *J. Climate*, **12**, 2397–2418.
- Jorgensen, D. P., and M. A. LeMone, 1989: Vertical velocity characteristics of oceanic convection. *J. Atmos. Sci.*, **46**, 621–640.
- , E. J. Zipser, and M. A. LeMone, 1985: Vertical motions in intense hurricanes. *J. Atmos. Sci.*, **42**, 839–856.
- Krueger, S. K., 1997: A GCS intercomparison of cloud-resolving models based on TOGA COARE observations. *Proc. New Insights and Approaches to Convective Parameterization*, Reading, United Kingdom, ECMWF, 113–127.
- Lafore, J.-P., J.-L. Redelsperger, and G. Jaubert, 1988: Comparison between a three-dimensional simulation and doppler radar data of a tropical squall line: Transport of mass, momentum, heat, and moisture. *J. Atmos. Sci.*, **45**, 3483–3500.
- Lin, X., and R. H. Johnson, 1996: Kinematic and thermodynamic characteristics of the flow over the western Pacific warm pool during TOGA COARE. *J. Atmos. Sci.*, **53**, 695–715.
- Lucas, C., E. J. Zipser, and M. A. LeMone, 1994: Vertical velocity in oceanic convection off tropical Australia. *J. Atmos. Sci.*, **51**, 3183–3193.
- Mapes, B. E., and R. A. Houze, 1992: An integrated view of the 1987 Australian monsoon and its mesoscale convective systems. *Quart. J. Roy. Meteor. Soc.*, **118**, 927–963.
- , and P. Zuidema, 1996: Radiative-dynamical consequences of dry tongues in the tropical troposphere. *J. Atmos. Sci.*, **53**, 620–638.
- Morcrette, J. J., 1991: Radiation and cloud radiative properties in the European center for medium range weather forecasts forecasting system. *J. Geophys. Res.*, **96**, 9121–9132.
- Numaguti, A., R. Oki, K. Nakamura, K. Tsuboki, N. Misawa, T. Asai, and Y.-M. Kodma, 1995: 45-day-period variation and low-level dry air observed in the equatorial western Pacific during TOGA COARE. *J. Meteor. Soc. Japan*, **73**, 267–290.
- Parsons, D., and Coauthors, 1994: The Integrated Sounding System: Description and preliminary observations from TOGA COARE. *Bull. Amer. Meteor. Soc.*, **75**, 553–567.
- , K. Yoneyama, and J.-L. Redelsperger, 2000: The evolution of the tropical western Pacific atmosphere–ocean system following the arrival of a dry intrusion. *Quart. J. Roy. Meteor. Soc.*, **126**, 517–548.
- Raymond, D. J., 1995: Regulation of moist convection over the western Pacific warm pool. *J. Atmos. Sci.*, **52**, 3945–3955.
- Redelsperger, J.-L., and G. Sommeria, 1986: Three-dimensional simulation of a convective storm: Sensitivity studies on subgrid parameterization and spatial resolution. *J. Atmos. Sci.*, **43**, 2619–2635.
- , and J.-P. Lafore, 1988: A three-dimensional simulation of a tropical squall line: Convective organization and thermodynamic vertical transport. *J. Atmos. Sci.*, **45**, 1334–1356.
- , and —, 1994: Non-hydrostatic simulations of a cold front observed during the FRONT 87 experiment. *Quart. J. Roy. Meteor. Soc.*, **120**, 519–555.
- , F. Guichard, and S. Mondon, 2000: A parameterization of mesoscale enhancement of surface fluxes for large-scale models. *J. Climate*, **13**, 402–421.
- Sherwood, S. C., 1999: Convective precursors and predictability in the tropical western Pacific. *Mon. Wea. Rev.*, **127**, 2977–2991.
- Sheu, R.-S., and G. Liu, 1995: Atmospheric humidity variations associated with westerly wind bursts during Tropical Ocean Global Atmosphere (TOGA) Coupled Ocean Atmosphere Response Experiment (COARE). *J. Geophys. Res.*, **100**, 25 759–25 768.
- Sommeria, G., 1976: Three-dimensional simulation of turbulent processes in an undisturbed trade wind boundary layer. *J. Atmos. Sci.*, **33**, 216–241.
- , and M. A. LeMone, 1978: Direct testing of a three-dimensional numerical model of the planetary boundary layer against experiment data. *J. Atmos. Sci.*, **35**, 25–39.
- Tompkins, A. M., and G. C. Craig, 1998: Radiative–convective equilibrium in a three-dimensional cloud-ensemble model. *Quart. J. Roy. Meteor. Soc.*, **124**, 2073–2097.
- Waugh, D. W., and L. M. Polvani, 2000: Climatology of intrusions into the tropical upper troposphere. *Geophys. Res. Lett.*, **27**, 3957–3860.
- Wei, D., A. M. Blyth, and D. J. Raymond, 1998: Buoyancy of convective clouds in TOGA COARE. *J. Atmos. Sci.*, **55**, 3381–3391.

- Yoneyama, K., and T. Fujitani, 1995: The behavior of dry westerly air associated with convection observed during the TOGA-COARE R/V Natushima cruise. *J. Meteor. Soc. Japan*, **73**, 291–304.
- , and D. B. Parsons, 1999: A mechanism for the intrusion of dry air into the tropical western Pacific region. *J. Atmos. Sci.*, **56**, 1524–1546.
- Zipser, E. J., 1977: Mesoscale and convective scale downdrafts as distinct components of squall line structure. *Mon. Wea. Rev.*, **105**, 1568–1589.
- , and M. A. LeMone, 1980: Cumulonimbus vertical velocity events in GATE. Part II: Synthesis and model core structure. *J. Atmos. Sci.*, **37**, 2458–2469.
- Zuidema, P., 1998: The 600–800-mb minimum in tropical cloudiness observed during TOGA COARE. *J. Atmos. Sci.*, **55**, 2220–2228.